



# Time Efficient Ultrasound Localization Microscopy Based on A Novel Radial Basis Function 2D Interpolation

Giulia Tuccio, Sajjad Afrakhteh, Giovanni Iacca, and Libertario Demi

**Abstract**— Ultrasound localization microscopy (ULM) allows for the generation of super-resolved (SR) images of the vasculature by precisely localizing intravenously injected microbubbles. Although SR images may be useful for diagnosing and treating patients, their use in the clinical context is limited by the need for prolonged acquisition times and high frame rates. The primary goal of our study is to relax the requirement of high frame rates to obtain SR images. To this end, we propose a new time-efficient ULM (TEULM) pipeline built on a cutting-edge interpolation method. More specifically, we suggest employing Radial Basis Functions (RBFs) as interpolators to estimate the missing values in the 2-dimensional (2D) spatio-temporal structures. To evaluate this strategy, we first mimic the data acquisition at a reduced frame rate by applying a down-sampling ( $DS = 2, 4, 8$ , and  $10$ ) factor to high frame rate ULM data. Then, we up-sample the data to the original frame rate using the suggested interpolation to reconstruct the missing frames. Finally, using both the original high frame rate data and the interpolated one, we reconstruct SR images using the ULM framework steps. We evaluate the proposed TEULM using four *in vivo* datasets, a Rat brain (dataset A), a Rat kidney (dataset B), a Rat tumor (dataset C) and a Rat brain bolus (dataset D), interpolating at the in-phase and quadrature (IQ) level. Results demonstrate the effectiveness of TEULM in recovering vascular structures, even at a  $DS$  rate of  $10$  (corresponding to a frame rate of sub-100Hz). In conclusion, the proposed technique is successful in reconstructing accurate SR images while requiring frame rates of one order of magnitude lower than standard ULM.

**Index Terms**— Frame rate, Super resolution, TEULM, ULM, 2D interpolation, RBFs.

## I. INTRODUCTION

ULTRASOUND is recognized as one of the principal medical imaging modalities for visualizing subcutaneous body structures such as organs, muscles, and arteries due to its safety, cost-effectiveness, and non-invasiveness [1]. However, conventional ultrasound performance is constrained by the diffraction limit, which constrains the spatial resolution to the scale of the wavelength [2], [3]. While at higher frequencies the spatial resolution improves, the beam's penetration depth

G. Tuccio, S. Afrakhteh, G. Iacca, and L. Demi (corresponding author) are with the Department of Information Engineering and Computer Science, University of Trento, Trento, Italy (email: giulia.tuccio@unitn.it, sajjad.afrakhteh@unitn.it, giovanni.iacca@unitn.it, libertario.demi@unitn.it)

Giulia Tuccio and Sajjad Afrakhteh contributed equally to this work.

diminishes, thus causing a trade-off between spatial resolution and penetration depth [2].

In the last decade, Ultrasound Localization Microscopy (ULM), namely a technique for visualizing the vasculature at unprecedented resolution, has addressed the aforementioned trade-off [4]. The super-resolved (SR) images obtained by ULM provide indispensable information for the understanding and diagnosis of various diseases that modify the vascular structure or blood flow, such as cancer [5]–[8], stroke [8], [9], and atherosclerosis [6]. ULM operates by individually localizing and tracking intravenously injected microbubbles (MBs), also known as ultrasound contrast agents (UCAs). The centroid of each MB can be localized with an accuracy 10 times lower than the wavelength [10], when UCAs are well separated. ULM is thus able to bypass the conventional ultrasonic diffraction limit by aggregating the centroid of single echoes produced by the UCAs [2], [11]. Finally, SR images are obtained by tracking the microbubbles as they flow through the vascular system, providing essential information about the vascular bed's structure as well as its flow dynamics [12].

Despite the advantages that ULM may bring in the clinical setting, its utilization is currently limited by two main practical considerations [2], [10], [13]. Firstly, low MBs concentrations and long acquisition times are necessary to record sufficiently separated MB echoes for localization and tracking [13]. Secondly, a high frame rate is necessary to coherently pair the MB signals from one frame to the successive one [14]–[16]. To date, this need for long acquisition times and high frame rates has hampered the ULM clinical translation.

Extensive research has been conducted to reduce the ULM acquisition time. One straightforward solution is to increase the concentration of MBs [17]. High concentrations, on the other hand, result in MB overlapping signals, making it impossible to discriminate between different MBs' echoes and individually localize them. To tackle this issue, various research works have been conducted, e.g. based on sparse recovery methods [18], [19], deconvolution [20], [21], and velocity filtering [2]. To distinguish overlapping MBs signals, Huang et al. [22] proposed establishing different sub-populations based on different flow patterns. However, these techniques require high frame rates that are generally not possible with the available clinical scanners. Other approaches take advantage of deep learning architectures to localize MBs in dense scenarios [23], [24]. However, deep learning necessitates a significant

amount of labeled data for model training and testing, which is difficult to obtain.

Moreover, Guo et al. [15] evaluated by a quantitative investigation the loss of ULM performance when decreasing the frame rate. The study demonstrates, by utilizing an in vivo dataset, that a decreased frame rate results in an unreliable microbubble detection and tracking, which in turn leads to a decreased spatial resolution (from  $9.9 \mu\text{m}$  to  $15 \mu\text{m}$  when going from 1kHz to 250Hz) as well as a decreased saturation (saturation drop above 50% from 1kHz to 100Hz). Furthermore, the frame rate has a significant impact on the precision of the velocity measurements.

To tackle the high frame rate requirement, Ackerman et al. [25] and Opacic et al. [26] implemented a modified Markov chain Monte Carlo data association to recover UCA tracks at a lower frame rate, which optimally associate MBs positions based on an underlying motion model. Another approach [27] uses a Kalman filter as a tracking backbone, and introduces MB image features on top. Although these approaches can recover UCAs tracks at a lower frame rate, their improved performance comes at a significant computational cost. Enabling lower frame rate acquisitions using TEULM would alleviate some of the data size constraints for ULM and would make the technology more pragmatic for clinical translation, where low frame rates are standard. To be more precise, adopting lower frame rate acquisitions in ULM can bring about numerous advantages in the clinical context. These benefits encompass reduced data size, compatibility with standard equipment, and cost-effectiveness.

In this study, we aim at bridging the gap between the high frame rates required by ULM (in the range of 1kHz) and the limited frame rate of the standard clinical scanners (in the sub-range of 100Hz).

To this end, we propose a new time-efficient ULM (TEULM) pipeline based on a novel 2-dimensional (2D) interpolation technique to relax the requirement on the high frame rate necessary to obtain super-resolved images. The article is structured as follows. Section II gives a detailed explanation of the interpolation technique used upstream the ULM pipeline. Next, we describe the key steps of ULM framework, as well as the TEULM pipeline. In the result section (Sec. III), we quantify the quality of the reconstructed images using TEULM, and compare these images with the SR images obtained through standard ULM. Finally, we provide the discussion and conclusions of the proposed method.

## II. MATERIALS AND METHODS

### A. RBF-based 2D interpolation

Radial Basis Functions (RBFs) have been frequently used in interpolate high-dimensional sparse data [28], advantage of this technique is that it delivers numerical results without entailing complicated computations. This makes it simple to apply to complicated geometries in a variety of spaces. In the following, we provide the formulation of the 2D interpolation problem using RBFs.

Given the data  $(\mathbf{X}_j, \mathbf{Y}_j)$ ,  $j = 1, 2, \dots, N$ , where  $\mathbf{X}_j$  and  $\mathbf{Y}_j \in \mathbb{R}^d$  (in our problem  $d = 2$ ), we aim to find

J是2D grid ( spatial temporal ) 上的 index

a continuous function  $S(\mathbf{X})$  so that  $S(\mathbf{X}_j) = \mathbf{Y}_j$ ,  $j \in \{1, 2, \dots, N\}$ . In addition, the interpolation bases are chosen as  $\{\phi(\mathbf{X} - \mathbf{X}_1), \phi(\mathbf{X} - \mathbf{X}_2), \dots, \phi(\mathbf{X} - \mathbf{X}_N)\}$ , where  $\mathbf{X}_1, \mathbf{X}_2, \dots, \mathbf{X}_N$  are predetermined interpolation nodes. These assumptions lead to the definition of RBFs as:

$$\phi(r_j) \equiv \phi(\|\mathbf{X} - \mathbf{X}_j\|) = \sqrt{\|\mathbf{X} - \mathbf{X}_j\|_2^2 + \tau^2} \quad (1)$$

where  $\|\cdot\|_2$  indicates the  $\ell^2$  norm (i.e., the Euclidean distance) and  $\tau$  represents the so-called shape parameter. Due to their radial dependence, these functions are referred to as RBFs. Some possible RBFs are listed in Table I.

**TABLE I:** RBF basis used in this study ( $\epsilon$  is a constant,  $r$  is the radius of the RBF, and  $\ln(\cdot)$  indicates the natural logarithm).

Method	Acronym	Formula
<b>Infinitely smooth</b>		
Multiquadric	MQ	$\phi(r) = \sqrt{1 + (\epsilon r)^2}$
Inverse multiquadric	IMQ	$\phi(r) = \frac{1}{\sqrt{1 + (\epsilon r)^2}}$
Gaussian	GA	$\phi(r) = e^{-\epsilon r^2}$
<b>Piece-wise smooth</b>		
Cubic	CU	$\phi(r) =  r ^3$
Thin plate spline	TPS	$\phi(r) = r^2 \ln r $

Following that, we develop a linear combination of RBFs  $\phi(r)$  to move forward with the 2D interpolation:

$$S(\mathbf{X}) = \sum_{j=1}^N \beta_j \phi(\|\mathbf{X} - \mathbf{X}_j^c\|_2, \tau), \quad (2)$$

where  $\mathbf{X} = (x_1, x_2, \dots, x_d)$ ,  $\tau$  is the shape parameter,  $\beta_j$  is the interpolation coefficient, and  $r = \|\mathbf{X}\|_2$ . If we intend to estimate  $f : \mathbb{R}^d \rightarrow \mathbb{R}$  utilizing the interpolators determined by Eq. (2), we need to find the interpolation coefficient N的长度是2D spatial-temporal grid的长度 do that, we use the following interpolation condition:

$$S(\mathbf{X}_j) = f(\mathbf{X}_j), \quad j = 1, 2, \dots, N. \quad (3)$$

By applying Eq. (3) at the central points of  $\mathbf{X}_j^c$  for  $j = 1, \dots, N$ , we obtain the linear system:

$$\Phi_{N \times N} \mathbf{B}_{N \times 1} = \mathbf{F}_{N \times 1} \quad \mathbf{B} = [\beta_1, \beta_2, \dots, \beta_N]^T \quad (4)$$

which can be expanded as follows

$$\underbrace{\begin{bmatrix} \phi(r_{1,1}) & \phi(r_{1,2}) & \dots & \phi(r_{1,N}) \\ \phi(r_{2,1}) & \phi(r_{2,2}) & \dots & \phi(r_{2,N}) \\ \vdots & \vdots & \ddots & \vdots \\ \phi(r_{N-1,1}) & \phi(r_{N-1,2}) & \dots & \phi(r_{N-1,N}) \\ \phi(r_{N,1}) & \phi(r_{N,2}) & \dots & \phi(r_{N,N}) \end{bmatrix}}_{\Phi} \underbrace{\begin{bmatrix} \beta_1 \\ \beta_2 \\ \vdots \\ \beta_{N-1} \\ \beta_N \end{bmatrix}}_{\mathbf{B}} = \underbrace{\begin{bmatrix} f(\mathbf{X}_1) \\ f(\mathbf{X}_2) \\ \vdots \\ f(\mathbf{X}_{N-1}) \\ f(\mathbf{X}_N) \end{bmatrix}}_{\mathbf{F}} \quad (5)$$

where  $\mathbf{X}_j$  indicates the imaging pixels,  $f(\mathbf{X}_j)$  refers to the pixel intensity of the imaging point  $X_j$ ,  $r_{i,j} = \|\mathbf{X}_i^c - \mathbf{X}_j^c\|$  is the Euclidean distance, and  $N$  is the number of points in the 2D grid (i.e., the imaging points in our problem).

Based on the system in Eq. (5), to solve the interpolation problem (i.e., finding the  $\beta$  values), we must invert the coefficient matrix  $\Phi$ , as discussed in the next section. Now, using the coefficients calculated from the above system, if we seek to

analyze the interpolator at  $M$  points  $\mathbf{X}_i$ ,  $i = 1, 2, \dots, M$ , the new coefficients matrix entries must be constructed as follows:  $h_{ij} = \phi(\|\mathbf{X}_i - \mathbf{X}_j^c\|_2) \forall j \in \{1, \dots, N\}$ . Finally, the following matrix multiplication is used to evaluate the interpolant at the  $M$  points:

$$\mathbf{F}_{est} = \mathbf{H}\mathbf{B} = \mathbf{H}\Phi^{-1}\mathbf{F}, \quad (6)$$

where  $\mathbf{F}_{est}$  represents the estimated  $\mathbf{F}$  (i.e., in our interpolation problem,  $\mathbf{F}_{est}$  indicates the interpolated data).

The invertibility of the interpolation matrix and the error analysis are described in Appendix A and B, respectively.

## B. Proposed Approach

**1) Standard ULM framework:** As shown in Fig. 1, the traditional ULM framework consists of five basic steps: data acquisition, pre-processing and filtering, MB detection, MB localization and tracking, and accumulation. For the data acquisition step, the standard framework demands data acquired at high frame rates. Following that, the high frame rate data is pre-processed to reduce clutter and tissue noise. In this study, we employ singular value decomposition (SVD) spatio-temporal filtering to distinguish the MBs signal from the surrounding tissue [30]. The SVD filter takes advantage of the fact that back-scatter tissue signals have a high spatio-temporal coherence compared to MB echoes. Therefore, by eliminating the initial  $k$  singular values, the tissue signal is filtered out from the data.

Next, MB signals are detected based on the pixels intensity in each frame. As in [17], an estimate of the number of MBs (i.e.,  $n$ ) in each frame is utilized instead of creating a threshold to identify the minimum pixel intensity value representative of the MB signals, which is non-trivial and may result in poor MB detection. In this paper, for each frame, the  $n$  pixels characterized by the most intense values are selected. Individual MBs are then localized using the Gaussian fitting algorithm [17], [31], [32], which fits a 2D multivariate Gaussian distribution. This approach assumes that the maximum intensity value ( $I$ ) in a grid of  $[N_z, N_x]$  pixels corresponds to the MB centroid. To recover the super-resolved location, the original image is up-sampled by a resolution factor  $res$ . Each pixel is interpolated into a  $res \times res$  grid, allowing to localize the MBs with a precision  $res$  times higher than the pixel size. The final image is then obtained as a grid of size  $[N_z \times res, N_x \times res]$ . Here, we define  $res$  as the empirical limit found in [17], namely 10. The localization problem can then be mathematically described as an optimization problem. After centering the subspace in the maximum value of the sub-sampled grid, the super-resolved z and x coordinates,  $(c_z, c_x)$ , of each MB is evaluated as the location of the Gaussian peak as follows:

$$\max I = \exp \left( - \left( \frac{(z - c_z)^2}{2\sigma_z^2} + \frac{(x - c_x)^2}{2\sigma_x^2} \right) \right), \\ (z, x) \in \left( \left[ -\left| \frac{f_z}{2} \right|, \left| \frac{f_z}{2} \right| \right], \left[ -\left| \frac{f_x}{2} \right|, \left| \frac{f_x}{2} \right| \right] \right), \quad (7)$$

where  $f_z$  and  $f_x$  respectively indicate the full width at half maximum (FWHM) along  $z$  and  $x$  directions. The standard deviations  $\sigma_z$  and  $\sigma_x$  are empirically evaluated to be equal to 1,

as in [17]. Then, the bipartite tracking algorithm matches each detected MB location in a frame-to-frame fashion. Thanks to their simplicity, the bipartite graph-based pairing methods are well established in the ULM context [13]–[17], [22], [27]. These algorithms solve the tracking problem through an optimal assignment, based on the MBS frame-to-frame distance. In particular, the relative distance between all the UCAs in two successive frames is evaluated. The MBs are then considered to be the same, or matched, in such a way that the total distance between all the MBs in the two frames is minimized. Since the assignment depends on the frame-to-frame distance, it is easy to understand the importance of a high frame rate to accurately pair MB signals [15], [16]. This paper implements a modified Khun-Munkres bipartite tracking algorithm, as in [33]. Generally, the method works on the assumption that each MB in one frame is paired with one MB in the subsequent frame. However, due to the uncertainty originated by the arbitrary estimation of the number of MBs in each frame in the localization step, the assumption may result in a sub-optimal solution. Furthermore, a sub-optimal solution might be caused by unpredictable UCAs events, such as MB appearance and/or disappearance. As such, the Khun-Munkres algorithm is modified to cope with partial assignment. In particular, a MB in a frame  $f$  which has depleted all the possible assignment options in the next frame  $f + 1$  is discarded [14]. Moreover, we establish a threshold for the minimum length of a track in order to further strengthen the robustness of the tracking performance, i.e., a track is discarded if it is lower than the threshold because it is considered as noise.

Finally, an SR intensity map is obtained by accumulating the tracks, previously smoothed and interpolated to fill in the missing points, over all frames. The velocity map, which defines a MB's velocity by its displacement over time, can also be retrieved and superimposed onto the SR intensity map.

**2) TEULM framework:** TEULM introduces, in the pre-processing stage, the RBF-based 2D interpolation technique to relax the frame rate required by standard ULM. The interpolation method aids in recovering the lost data, which is the result of adopting a reduced frame rate acquisition. More specifically, we propose sparse (low frame rate acquisition) combined with 2D interpolation to reconstruct the unknown information corresponding to the frames that are not recorded in the low frame rate acquisition (i.e., for a given down-sampling (DS) rate, interpolating  $DS - 1$  middle frames to achieve high frame rate IQ data needed for high-quality SR imaging). Following that, we adopt the standard ULM framework, described in Section II-B.1. We pre-process the interpolated data by applying SVD filer first, keeping the  $k$ -values used for filtering as the original ones, and successively a Butterworth filter. Then TEULM's framework comprises of detection, localization and tracking of the MBs. The final images are then obtained through accumulation (see Fig. 1). ULM and TEULM parameters are summarized in Table III. In the case of using ULM at the original frame rate and TEULM, we use the same parameters used in [17]. However, for the ULM at down-sampling rates  $> 1$  (non-interpolated data), we adapt the maximum linking distance and minimum track length by a factor that is proportionate to the level of down-

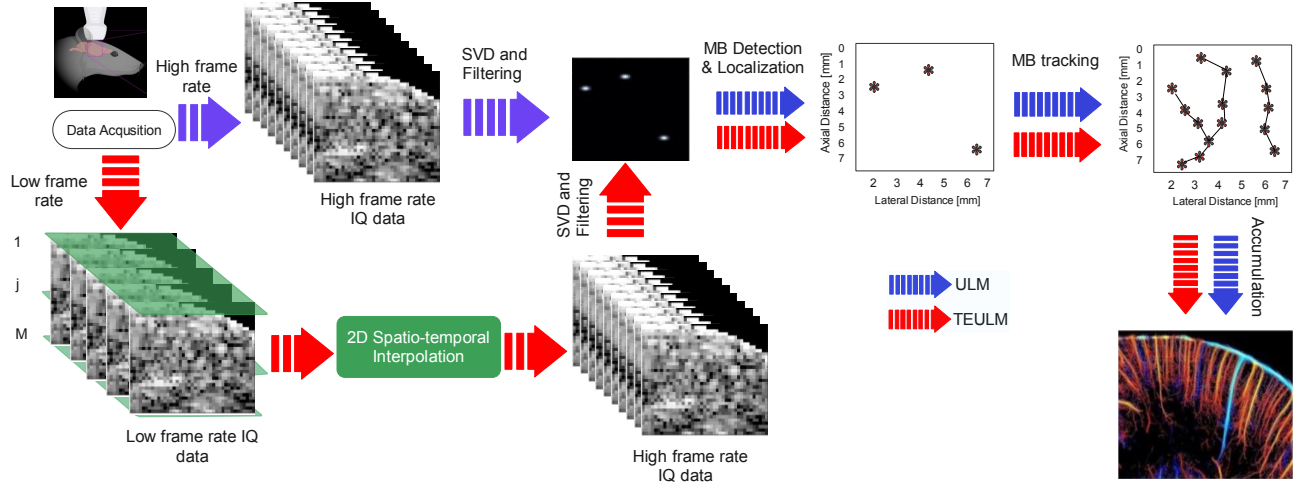


**Fig. 1:** Main processing steps of Ultrasound Localization Microscopy (ULM) and Time Efficient Ultrasound Localization Microscopy.

sampling. For example, when down-sampling by a factor of 2 ( $DS=2$ ), the maximum linking distance is adjusted to be twice the original linking distance, while the minimum track length is set to half of its original value. This adjustment is made for a fair comparison, which accounts for the fewer frames used yielding in larger gaps between microbubble positions in consecutive frames. Similarly, due to the reduced number of frames, a shorter minimum track length is necessary.

**TABLE II:** Datasets summary in this study.

Dataset	MB Dose	Tilted Angles
Rat Brain Infusion (dataset A)	400 $\mu$ l	(-3°; 0°; 3°)
Rat Kidney Bolus (dataset B)	500 $\mu$ l	(-10°; -5°; 0°; 5°; 10°)
Rat Tumor Bolus (dataset C)	100 $\mu$ l	(-10°; -5°; 0°; 5°; 10°)
Rat Brain Bolus (dataset D)	400 $\mu$ l	(-5°; 0°; 5°)

### C. Data

To assess the proposed strategy, we use four *in vivo* datasets. We denote the *in vivo* datasets as dataset A for the Rat Brain, dataset B for the Rat Kidney, dataset C for the Rat tumor and dataset D for the Rat Brain bolus.

The datasets, presented in [17] and summarized in Table II, are recorded with a 15 MHz center frequency probe (Vermon, France). We opted for the use of *in vivo* datasets due to their capacity to encompass a wide range of hemodynamic structures across different organs (such as the brain and kidney) and various injection modalities.

### D. In vivo evaluation metrics

We use the following metrics to evaluate the TEULM-generated SR image quality and compare it with that obtained by standard ULM.

1) **Root Mean Square Error (RMSE):** The similarity between the original image, reconstructed at 1KHz ( $I_1$ ), and the images

**TABLE III:** ULM and TEULM parameters used in this work.

\* and \*\* indicate the parameters which were adjusted for the non-interpolated data (ULM at  $DS > 1$ ). In particular, \* and \*\* respectively multiply and divide by a factor equal to the DS rate used.

Dataset	Frame Rate (Hz)	k-value (SVD)	Max. Linking Distance*	Min. Track length**	Number of MB / Frame
Dataset A	1000	5	2	15	70
Dataset B	1000	10	1.5	15	100
Dataset C	500	10	1	10	100
Dataset D	1000	10	2	10	100

interpolated at different  $DS$  rates ( $I_{DS}$ ), with  $DS = 2, \dots, 10$ , is assessed pixel-by-pixel using the root mean square error:

$$RMSE = \sqrt{\sum_{i=1}^{N_{pix}} \frac{(|I_{DS} - I_1|)^2}{N_{pix}}}, \quad (8)$$

where  $N_{pix}$  denotes the total number of pixels in the reconstructed image. Both density maps, which depict the vascular anatomy, and velocity maps are evaluated. The Root Mean Square Error (RMSE) is employed to gauge the resemblance in terms of vascular structure and intensity among the reconstructed images acquired through TEULM and ULM at various levels of  $DS$  rates. Indeed, the RMSE conducts a pixel-level assessment of the error, taking into account the image reconstructed from the initial high frame-rate data (1KHz for datasets A, B, and D, and 500Hz for dataset C) as the reference standard.

2) **DICE score:** The DICE score evaluates the similarity between two images by measuring the overlapping area of two images over the area of their union [34]:

$$DICE = \frac{2 \times |I_{DS} \cap I_1|}{|I_{DS}| \cup |I_1|}, \quad (9)$$

The DICE score quantitatively assesses the resemblance of the reconstructed binary images generated by ULM and TEULM across various  $DS$  rates.

**3) Percentage of preserved tracks:** Since the number of detected tracks has a significant impact on the saturation and on the quality of the reconstructed images, we analyze the statistics related to the number of tracks at various  $DS$  rates. The ratio of the number of tracks found at the various  $DS$  rates ( $DS = 2, \dots, 10$ ) to those found at  $DS=1$  is used to calculate the percentage of preserved tracks. The percentage of preserved tracks is evaluated for density maps only. In ULM, a density map refers to a spatial representation of vessel density within a region of interest.

**4) Saturation:** We further assess the TEULM performance at different  $DS$  rates through saturation (i.e., indicating the number of pixels crossed by MBs) [15], [16]. The evaluation of the saturation is meaningful since the reconstructed images are the result of the accumulation of the pixels crossed by the MBs. In this study, the saturation curve is calculated as the percentage of filled pixels over the total area of the image. The saturation is evaluated only for density maps.

**5) Fourier Ring Correlation (FRC):** Fourier Ring Correlation is a commonly used method in the ULM context to estimate the spatial resolution of the super-resolved images [35]. The  $FRC$  evaluates the spatial frequency correlation along iso-spatial frequency rings ( $R$ ) between two sub-images in the frequency domain, formed by random splitting the tracks:

$$FRC(R) = \frac{\sum_{ring} F_1(R)F_2(R)^*}{\sqrt{\sum_{ring} |F_1(R)|^2 \sum_{ring} |F_2(R)|^2}}, \quad (10)$$

The resolution is the inverse value of the  $FRC$  curve, when the  $FRC$  drops below the threshold value. In this study, we select the 1/2 bit as thresholding method, which corresponds to the highest spatial frequency necessary to collect the information to fill half a bit [36], [37]. To achieve an unbiased and objective quantification, we conduct global (i.e., whole image)  $FRC$  resolution estimates.

### III. RESULTS

In this section, we present the results obtained through TEULM using the *in vivo* datasets described in section II-C.

We provide the *in vivo* results of standard ULM on the original high frame rate data (namely, 1kHz for dataset A, B and D and 500Hz for dataset C), see Fig. 2. These images are considered as a reference. Figures 3, 4, 5, and 6 depict the ULM and TEULM reconstructed density and velocity maps for datasets A, B, C, and D, respectively, across different  $DS$  rates. It's worth emphasizing that for dataset C, we provide the results until down-sampling 6 (which implies a frame rate of 83Hz) which demonstrates the capability of our proposed TEULM approach to the frame rates close to the current clinical system's frame rate. In addition, it should be noted that conventional ULM fails to reconstruct any tracks using a higher down-sampling ( $DS \geq 7$ ). The results show that for  $DS \geq 2$ , TEULM performs better than standard ULM in recovering the local and global information (i.e., ULM even fails to recover the global information at higher  $DS$  rates). As expected, a decrease in the frame rate (from left to right) results in a proportional degradation in the image quality. Qualitatively, the vessel definition appears to be less

continuous and more blurry at higher  $DS$  rates compared to the original images, see Fig. 2. We quantitatively assess this loss of definition in TEULM's generated density maps through the spatial resolution obtained using  $FRC$  on the entire image (Table IV), for all the *in vivo* datasets. The Fourier Ring Correlation evaluates the spatial resolution as the correlation between 2 sub-images formed by randomly splitting the tracks forming the density maps. In addition, we evaluate the consistency of the density maps generated by TEULM and ULM with the ones obtained using the high frame rate data using the DICE score, see Table V. For all the *in vivo* datasets, we further evaluate the efficiency of the proposed technique by means of two of the previously introduced metrics: the percentage of preserved tracks, and the saturation. The metrics are shown in Fig. 8 considering down-sampling 2, 4, 8 and 10. Fig. 8 clearly shows that TEULM preserves the majority of the tracks, as well as a constant saturation level compared to ULM, for which both the metrics decrease exponentially with increasing down-sampling.

**TABLE IV:** Spatial resolution (in  $\mu\text{m}$ ) measured by the  $FRC$  curve and the 1/2 bit thresholding method for the high frame rate ULM (1KHz for datasets A, B and D and 500Hz for dataset C) and TEULM at different  $DS$  rates for the *in vivo* datasets.

	Original	$DS = 2$	$DS = 4$	$DS = 8$	$DS = 10$
Dataset A	11.49	10.27	11.35	14.5	17.8
Dataset B	26.3	25.71	27.9	28.6	30.3
Dataset C	24.75	25.8	26.52	30.95	33.11
Dataset D	13.9	12.94	13.74	19.72	20.08

When under-sampling, we can generate multiple datasets from the high frame rate data. To assess the consistency across different datasets, we generate the permutation starting from frame 6 at down-sampling of 10 and compare the results with respect to the dataset generated starting from frame 1. The choice of the permutation allows us to evaluate the performance of the proposed approach for the most asynchronous couple of data that we could generate. Particularly, we assess the performance of TEULM through the statistical results (mean  $\pm$  standard deviation) of the  $DICE$  score, the saturation percentage, and the percentage of preserved tracks. The results of the  $DICE$  score are presented in Table V. The percentage of preserved tracks for dataset A, B, C, and D is  $0.98 \pm 7 \times 10^{-4}$ ,  $0.77 \pm 4 \times 10^{-2}$ ,  $0.37 \pm 1 \times 10^{-2}$ , and  $0.83 \pm 2 \times 10^{-2}$ , respectively. In addition, the saturation percentage reaches the value of  $0.96 \pm 2 \times 10^{-2}$ ,  $0.68 \pm 1 \times 10^{-2}$ ,  $0.77 \pm 3 \times 10^{-2}$ , and  $0.9 \pm 1 \times 10^{-2}$  for dataset A, B, C, and D, respectively. The results certify the consistency of TEULM across permutations.

In addition, we analyze the influence of the frame rate on the velocity maps obtained with TEULM and ULM. To this end, we calculate the flow direction and the velocity magnitude maps for the *in vivo* datasets. For the rendering of the flow direction of the blood flow, we use the red and blue colors to encode the different directions (see second row of Figs. 3, 4, 5, and 6, for dataset A, B, C and D respectively). About the mean velocity magnitude encoding (see the third row of Figs. 3, 4, 5, and 6, for dataset A, B, C and D respectively), the slowest

**TABLE V:** *DICE* score for all the *in vivo* datasets of ULM and TEULM density maps.  $\star$  indicates that for TEULM at  $DS=10$ , we present the mean and the standard deviation of the *DICE* score with respect to two permuted datasets.

Dataset	Method	DS rates			
		2	4	8	$10^{\star}$
Dataset A	TEULM	0.90	0.87	0.8	$0.79 \pm 5 \times 10^{-4}$
	ULM	0.78	0.60	0.29	0.19
Dataset B	TEULM	0.87	0.85	0.82	$0.81 \pm 1 \times 10^{-4}$
	ULM	0.76	0.49	0.20	0.14
Dataset C	TEULM	0.72	0.72	0.69	$0.68 \pm 7 \times 10^{-5}$
	ULM	0.43	0.21	-	-
Dataset D	TEULM	0.91	0.89	0.84	$0.82 \pm 2 \times 10^{-4}$
	ULM	0.82	0.73	0.58	0.52

velocities are encoded in blue, whereas the high velocities are encoded in red. The results of the velocity profiles, provided in row two and three of the Figures 3 (dataset A), 4 (dataset B), 5 (dataset C), and 6 (dataset D), clearly show that there is a lower limit to the frame rate reduction under which it is not possible to recover the global and local velocity information of the vascular structure.

Moreover, we quantify the error for both the intensity and velocity maps of the sparse ULM and TEULM with respect to the original ULM (i.e., obtained with a frame rate equal to 1kHz for dataset A, B and D and frame rate equal to 500Hz for dataset C) utilizing the *RMSE* metric (Figure 7). The results allow us to evaluate the trend of these two metrics with respect to different *DS* rates, up to 50Hz<sup>1</sup>.

Finally, we have conducted an evaluation of the mean velocity profiles for all the *in vivo* datasets (see Fig. 9). These profiles represent the mean velocity values (in mm/s) against the number of tracks associated with each mean velocity across all the tracks within their respective datasets. Fig. 9 shows that the mean velocities are misestimated at higher down-sampling, confirming that recovering the dynamic profile is a challenging task for the RBFs interpolators.

#### IV. DISCUSSION

The primary goal of this study is to present an innovative approach to enable ULM at low frame rates, which will facilitate ULM clinical translation. In this regard, we propose a modified ULM framework, called TEULM, that can cope with low frame rate data by employing the suggested 2D interpolation technique.

The proposed technique has been tested on four pre-clinical *in vivo* data (dataset A, B, C and D). For the *in vivo* datasets, we demonstrate the high efficiency of TEULM in recovering the information lost when using a low frame rate (Figures 3, 4, 5 and 6, for datasets A, B, C and D respectively). More specifically, while both TEULM and ULM face an image quality loss at lower frame rates, as we can see in Figures 3, 4, 5 and 6, the extent of the loss varies significantly between the two techniques. In other words, the vessel's appearance for ULM degrades quickly. For instance, at a frame rate lower than 250Hz, the vascular structure is almost unrecognizable for all the datasets, which shows the ULM's low performance at

lower frame rates. In contrast, when using TEULM, the overall vascular structure remains unchanged. Besides, an increase in the *DS* rate results in a loss of vascular definition, manifested by more blurry areas, mostly in the fine vasculature (See an example shown in the magnified Region of Interest (ROI) in Fig. 4 and highlighted by the green box. This loss of definition is quantitatively assessed by the spatial resolution estimates using the *FRC* (Table IV). Despite the loss in spatial resolution, the saturation and the percentage of preserved tracks are invariant in the reconstructed images using the suggested TEULM method (see Fig. 8). Further, for dataset B, we observe the appearance of vascular structures in TEULM at  $DS = 10$ , i.e., 100Hz, (Fig. 4 highlighted by the yellow arrow) that are absent in the original frame rate, i.e., 1KHz (see Fig 2). It should be noted that, in the absence of the ground truth, it is difficult to judge whether the appearing vascular structures are artifacts or real vessels. Nevertheless, we observe that for the dataset B the global bloodstream structure in the proposed TEULM is not substantially impacted by either the loss of definition or the emergence of vascular artifacts, resulting in a *DICE* score of 0.81 at  $DS = 10$ . In Table V we provided the *DICE* score values for the *in vivo* datasets, which allows to quantitatively evaluate TEULM's performance in recovering the vessel's structure at a lower frame rate. The minimum *DICE* score values (at  $DS = 10$ ) obtained using TEULM are 79%, 81%, 68% and 82% for dataset A,B,C and D, respectively. TEULM's high *DICE* scores show the effectiveness of the suggested technique in reconstructing the missing information. On the other hand, ULM demonstrates poor *DICE* similarity indices (19%, 14% and 52% for dataset A, B and D respectively), which could be justified by the failure of the tracking algorithm at lower frame rates. Thus, for ULM, in regions characterized by complex structures (e.g. crossing vessels or junctions) the algorithm falsely pairs MBs, resulting in unreliable vessel depiction. This assumption would also explain why dataset B and C has a much lower similarity compared to dataset A and D. It seems in fact that the vasculature of the kidney and tumor (dataset B and C) is much more tortuous and characterized by short vessels, which are easily lost at lower frame rates.

The reason behind ULM's poor performance at low frame rates can be attributed to the tracking algorithm, which significantly relies on the frame rate as it employs a frame-by-frame matching approach. In other words, with a decrease in the frame rate, MBs may be discarded due to the inability to find the correct match in successive frames. Consequently, several tracks are not found or rejected because of an insufficient amount of known information, leading to a decrease in saturation and vessel definition. In fact, the number of preserved tracks in ULM for both datasets decreases exponentially as we increase the *DS* rate. As can be seen in Figs. 8, which presents the saturation curve and the percentage of recovered tracks at different frame rates for datasets A, B, C and D, in comparison to the original image. Additionally, at the lower frame rates, the saturation curves clearly show a decline in the ULM's capability to reconstruct the vasculature (i.e., at a *DS* rate of 5, the saturation on all the *in vivo* datasets decreases by more than the 50%).

<sup>1</sup>Intensity maps available in the link.

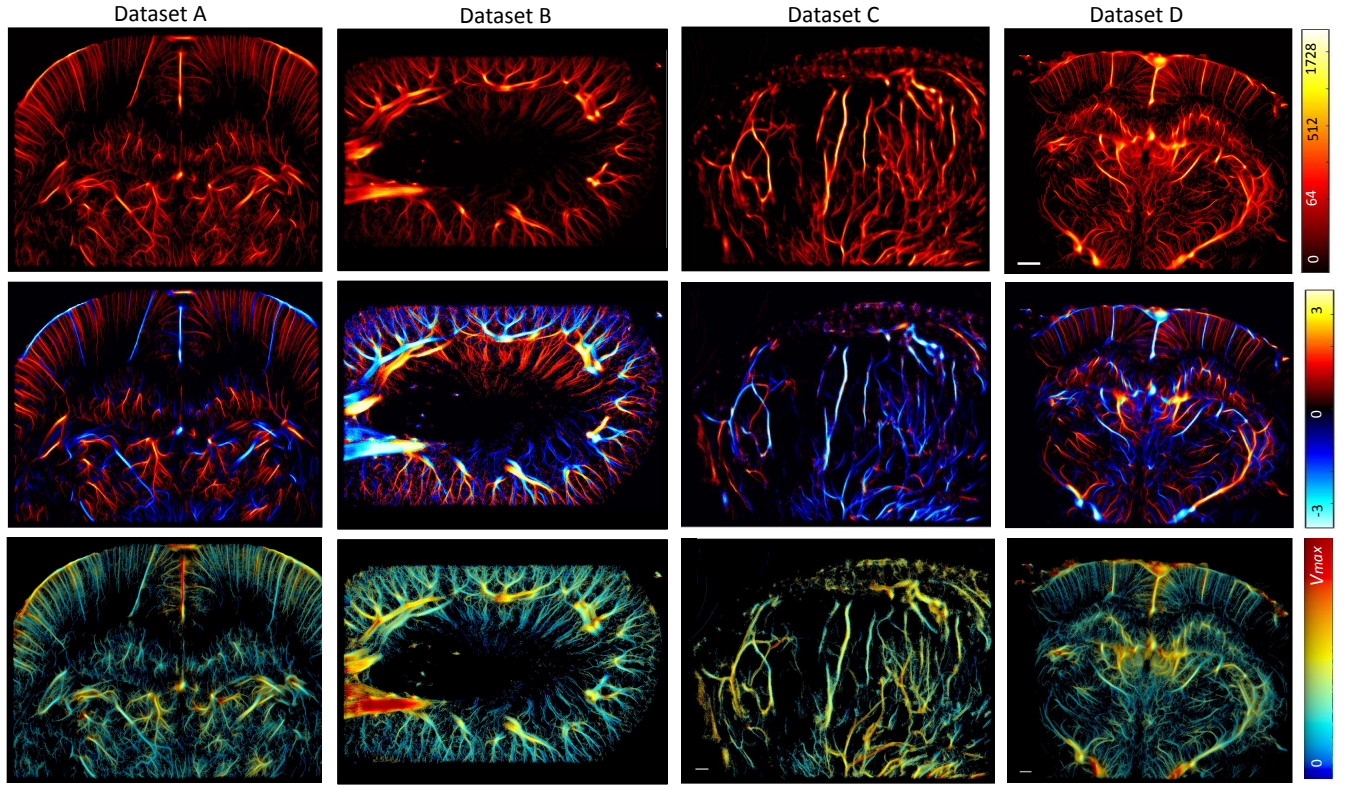


**Fig. 2:** Reconstructed density maps (first row), flow direction map (second row) and velocity magnitude maps (third row) for the *in vivo* datasets using the original high frame rate data (1kHz for dataset A, B and D and 500Hz for dataset C). The colorbar of the density maps shows the number of counts of MBs centroids found in each pixel of the image. The colorbar of the Flow direction map indicates values in  $MBs/(pix.sec)$ . The Velocity magnitude color-map encodes different mean velocities. Red corresponds to the maximum velocity ( $V_{max}$ ) of 70 mm/s, 40 mm/s, 48 mm/s and 63 mm/s for dataset A, B, C and D, respectively).

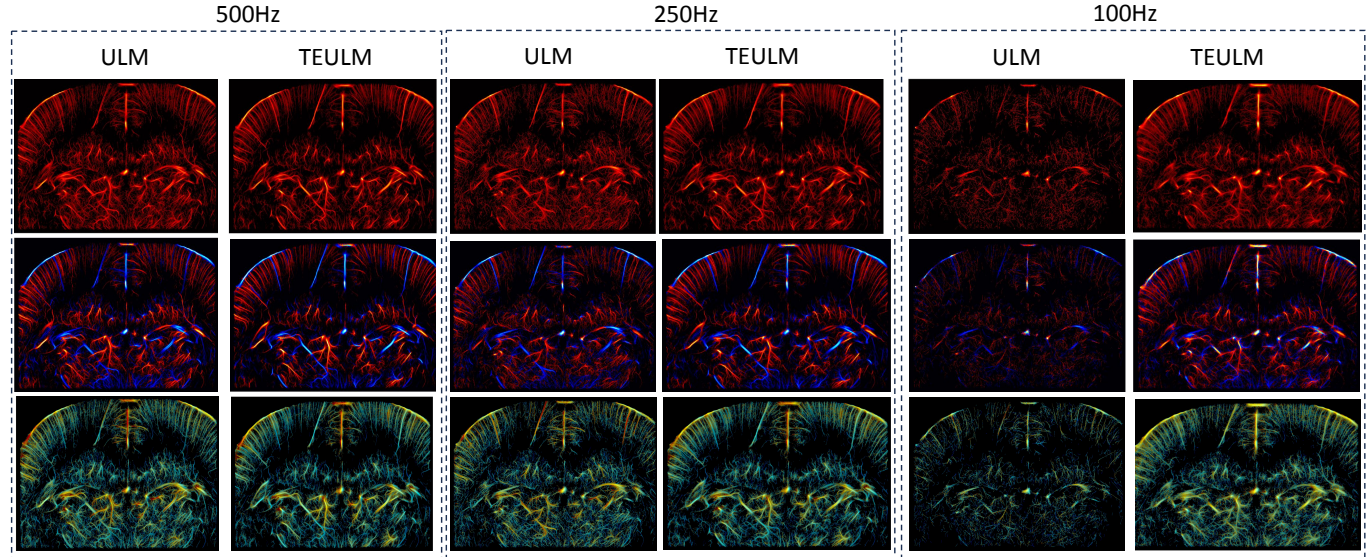


**Fig. 3:** ULM- and TEULM-generated density maps (first row), flow direction map (second row), and velocity magnitude map (third row) for Dataset A at different frame rates of 500Hz ( $DS=2$ ), 250Hz ( $DS=4$ ) and 100Hz ( $DS=10$ ). The color bar of the figure is the same as original ones in Fig. 2.

TEULM, on the other hand, maintains a high percentage of recovered tracks. The value remains consistently around 1 for

dataset A and approximately 0.85 for dataset D across all  $DS$  rates. However, we do notice a reduction in the percentage of

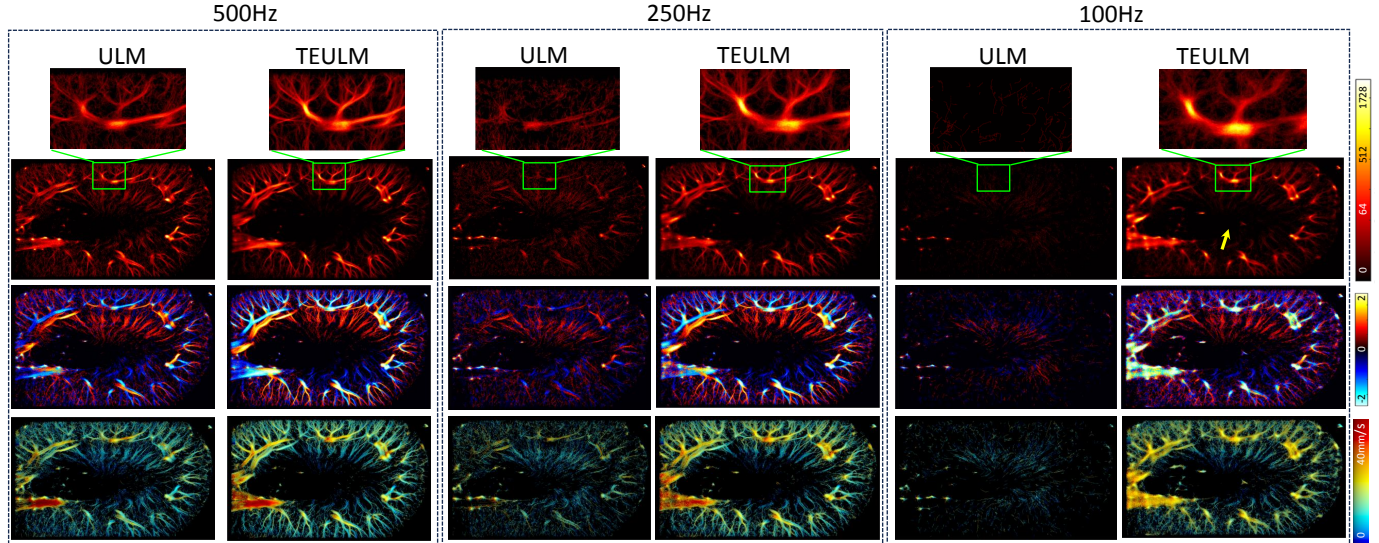


**Fig. 4:** ULM- and TEULM-generated density maps (first row), flow direction map (second row), and velocity magnitude map (third row) for Dataset B at different frame rates of 500Hz ( $DS = 2$ ), 250Hz ( $DS = 4$ ) and 100Hz ( $DS = 10$ ). The color bar of the figure is the same as original ones in Fig. 2.

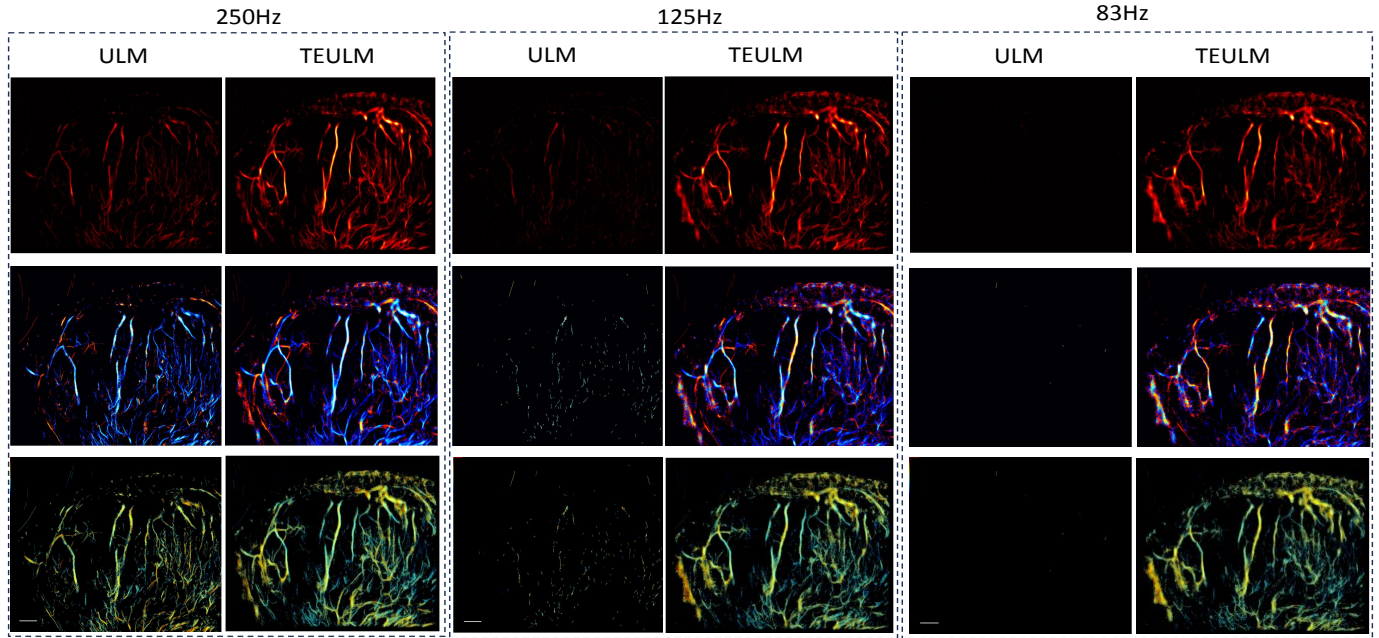


**Fig. 5:** ULM- and TEULM-generated density maps (first row), flow direction map (second row), and velocity magnitude map (third row) for Dataset C at different frame rates of 250Hz ( $DS = 2$ ), 125Hz ( $DS = 4$ ) and 83Hz ( $DS = 6$ ). We have presented images up to a  $DS$  rate of 6 because, at higher  $DS$  rates, ULM is unable to recover any tracks. The color bar of the figure is the same as original ones in Fig. 2.

preserved tracks at  $DS=6$  for dataset B and  $DS=4$  for dataset C. Nevertheless, TEULM's ability to preserve the number of tracks is reflected by the saturation of the density maps. The saturation levels for datasets A, B, and D remain consistently near 95%, while dataset C exhibits a saturation level of around 80%, when compared to the SR image generated using the original high frame rate data. The number of preserved tracks and saturation percentage indicate that datasets B and C are more challenging for TEULM. There might be a physiological

reason for this. In fact, dataset B relative to the Rat Kidney and dataset C representative of the Rat Tumor are characterized by shorter and broken tracks, which are more difficult to recover when using a higher  $DS$  rates.

TEULM and ULM super-resolution density and velocity maps are further evaluated through the  $RMSE$  at different  $DS = 2, 4, 8, 10$  rates (shown as a heatmap in Fig. 7). In both TEULM and ULM, the error, which is color-coded, exhibits an upward trend as the down-sampling rate increases. When

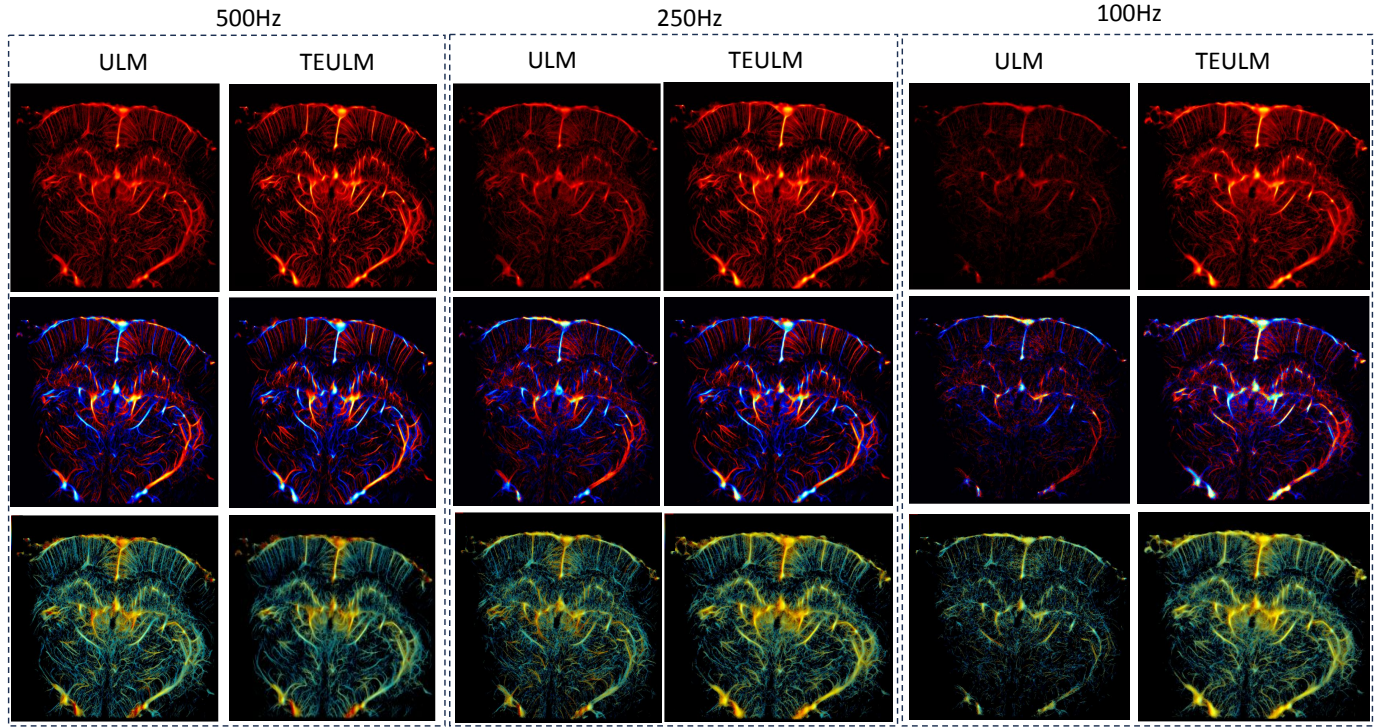


**Fig. 6:** ULM- and TEULM-generated density maps (first row), flow direction map (second row), and velocity magnitude map (third row) for Dataset D at different frame rates of 500Hz ( $DS=2$ ), 250Hz ( $DS=4$ ) and 100Hz ( $DS=10$ ). The color bar of the figure is the same as original ones in Fig. 2.

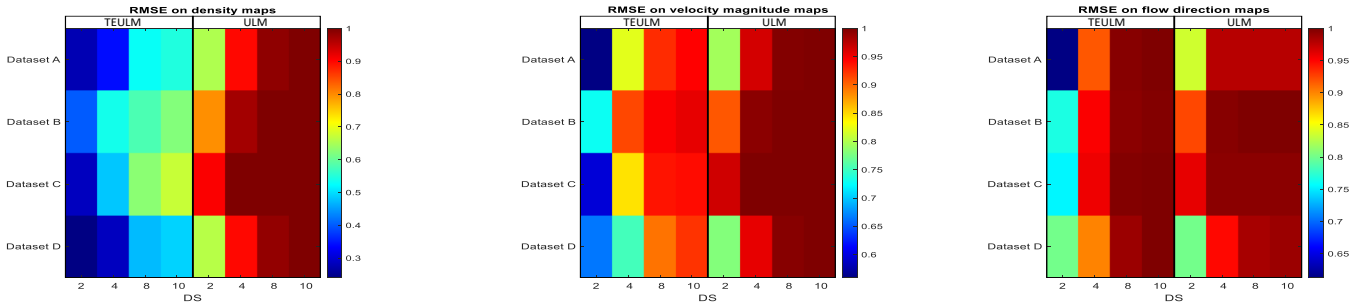


**Fig. 7:** Heatmaps representing the normalized Root Mean Square Error (RMSE) of the reconstructed density and velocity maps at  $DS=2, 4, 8, 10$  for TEULM and ULM for the *in vivo* datasets (A, B, C and D). The RMSE is normalized with respect to the maximum value for each dataset.

examining TEULM's density maps *RMSE* across all the *in vivo* datasets, it is noteworthy that the error gradient gradually rises. Remarkably, it appears that this gradient has not yet reached a plateau. Specifically, the *RMSE* remains below 50% for all datasets when employing TEULM, whereas it surpasses 80% when using ULM. This observation implies the potential for further increasing the *DS* value. In contrast, the error gradient for ULM stabilizes rapidly, particularly for dataset C (it's important to mention that ULM cannot recover any tracks with a *DS* greater than 6). This phenomenon underscores ULM's challenge in accurately reconstructing the morphology of vessels in a clinical setting marked by limited frame rate acquisition capabilities.

We investigated the efficacy of TEULM in reconstructing flow dynamics in terms of axial velocity and its magnitude. The maps of the axial velocity and velocity magnitude for the

*in vivo* datasets are given in rows two and three of Figs. 3 (dataset A), 4 (dataset B), 5 (dataset C) and 6 (dataset D). The results confirm that recovering the flow dynamics is a more challenging task even when using TEULM, due to the loss of spatio-temporal information at lower frame rates. At *DS* rates greater than 4 we observe high deviations in the flow direction information even in larger vessels. TEULM's poor performance in recovering the velocity information is further highlighted by the *RMSE* evaluated on the velocity magnitude and flow direction maps for the *in vivo* datasets presented in Fig. 7. In particular, the error reaches above the 80% already at *DS*=4 for all the datasets when using TEULM, and above 95% when using ULM.

Furthermore, TEULM misestimates the velocity magnitude, which tends to become more homogeneous as the *DS* rate increases for all the datasets, as seen in Figs. 3, 4, 5 and 6, for

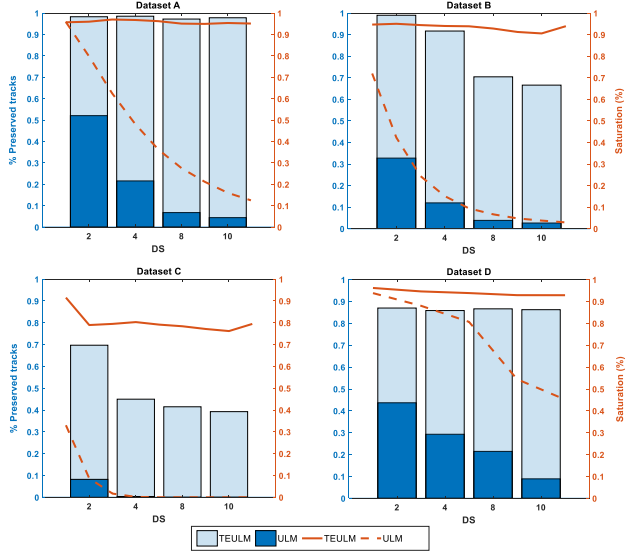


**Fig. 8:** Variation of the percentage of preserved tracks (shown as bar plots) and the percentage of saturation (shown as line plot) versus the changes in  $DS$  rate (for the *in vivo* datasets). The results are normalized with respect to the tracks and the saturation of the reconstructed images using the high frame rate datasets, corresponding to 1KHz for Dataset A, B and D, and 500Hz for Dataset C. For dataset C, since ULM fails to recover any track for  $DS > 7$ , the saturation and the number of preserved tracks in equal to 0.

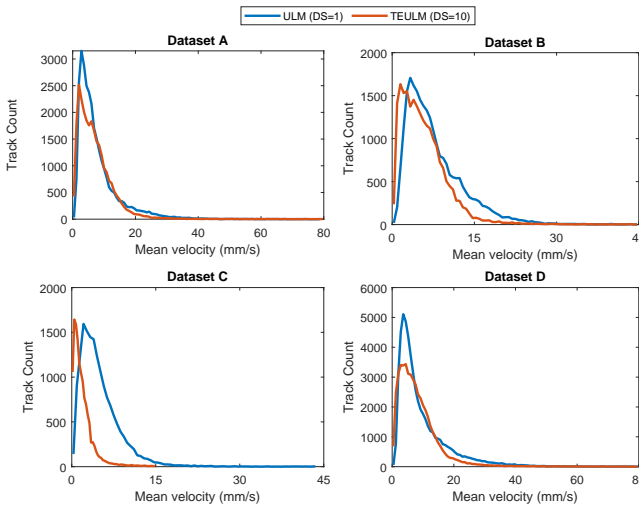


**Fig. 9:** Mean velocities (mm/s) evaluated for ULM at the original frame rate and TEULM at down-sampling rate 10, for all the *in vivo* datasets.

datasets A, B, C and D respectively. The loss of the magnitude information may be explained by the reduced amount of information available at lower frame rates, which yields to a loss of short micro-vessels, as well as a loss of longer tracks, which become shorter. To further analyze the velocity misestimation phenomena, we evaluate the mean velocity across all the tracks within their respective datasets in Fig. 9). As can be seen from the figure, there is a noticeable decrease in mean

velocities for the down-sampling rate of 10 for all the *in vivo* datasets. The results clearly indicate that accurately estimating velocities becomes a formidable challenge at lower frame rates, particularly when the microbubbles are moving at high speeds. Consequently, this leads to inaccuracies in velocity estimation. Moreover, the tracking algorithms heavily rely on both spatial and temporal information to match microbubbles across frames. In our current approach, the interpolation technique utilizes spatial and temporal information along a 2D plane to reconstruct the missing frames, see Fig. 1. Hence, we believe that implementing a 3D interpolation technique has the potential to enhance the accuracy of velocity estimation. This approach may better capture the intricate dynamics of microbubble movement and improve the overall performance of the tracking process.

Another consideration concerns the clinical utility of TEULM. The proposed TEULM represents a step towards transitioning ULM into clinical practice, addressing the current constraint of high frame rate requirements. However, despite the striking similarity in global information between the SR images reconstructed at  $DS=10$  using TEULM and those obtained through high frame rate ULM, we observe a substantial loss in the definition of vessels, particularly in the intricate microvascular structure. This loss may adversely affect both the quantity and quality of clinical information within the SR images. Furthermore, we note a marked decline in the retrieval of dynamic information at  $DS$  values exceeding 4, which imposes a limitation on TEULM's applicability in clinical scenarios. Therefore, if these SR images are to be used in a clinical context, we assert the need for further enhancements in the representation of vessels within the microvasculature and in the recovery of dynamic information at sub-100Hz frame rates before considering the extension of utilization with higher  $DS$  factors.

There are some limitations that are not explored in the study. First, in this paper, we only tested TEULM on 2D datasets. As future work, we envision extending the proposed approach to a 3D dataset, since 3D TEULM would represent an additional and fundamental step towards facilitating the clinical translation of this technology.

Second, the impact of motion on TEULM performance has not been explored in this paper. However, motion may lead to errors in reconstructing the signal path and target localization when using higher  $DS$  rates. Therefore, addressing motion effects through the implementation of motion compensation techniques could be explored as a potential avenue for future research. In addition, we aim at implementing a 3D interpolation technique. We anticipate that this approach will enhance the performance of TEULM in capturing dynamic profiles, even at lower frame rates.

## V. CONCLUSION

This study presents TEULM, a technique to alleviate the high frame rate data acquisition (in the range of 1kHz), generally necessary to frame-to-frame pair the microbubbles in the ULM framework. Relaxing such constraint would promote the ULM clinical transition, as the US systems used in hospital

can reach a frame rate of a magnitude lower. Results show that TEULM allows the generation of SR density maps with data acquired at frame rates as low as 50 Hz (an order of magnitude lower than the standard ULM). On the other hand, even if still capable to relax the frame rate by factor 4, TEULM required slightly higher frame rates (250 Hz) for the generation of consistent velocity maps with respect to the high frame rate's generated maps.

## REFERENCES

- [1] P. G. Newman and G. S. Rozicki, "The history of ultrasound," *Surgical Clinics of North America*, vol. 78, no. 2, pp. 179–195, 1998.
- [2] U. Soylu and Y. Bresler, "Circumventing the resolution-time trade-off in ultrasound localization microscopy by velocity filtering," 2021, arXiv:2101.09470.
- [3] A. Ng and J. Swanevelder, "Resolution in ultrasound imaging," *Continuing Education in Anaesthesia Critical Care & Pain*, vol. 11, no. 5, pp. 186–192, 08 2011.
- [4] O. Couture, B. Besson, G. Montaldo, M. Fink, and M. Tanter, "Microbubble ultrasound super-localization imaging (musli)," in *IEEE International Ultrasonics Symposium, IUS*, 10 2011, pp. 1285–1287.
- [5] S. Dencks, M. Piepenbrock, T. Opacic, B. Krauspe, E. Stickeler, F. Kiessling, and G. Schmitz, "Clinical pilot application of super-resolution us imaging in breast cancer," *IEEE transactions on ultrasonics, ferroelectrics, and frequency control*, vol. 66, no. 3, pp. 517–526, 2018.
- [6] H. Yi, M. Lowerison, P. Song, and W. Zhang, "A review of clinical applications for super-resolution ultrasound localization microscopy," *Current Medical Science*, vol. 42, no. 1, Feb. 2022, funding Information: This study was supported by the National Cancer Institute (NCI) of the National Institutes of Health (NIH) under Award (No. R00CA214523). The content is solely the responsibility of the authors, and does not necessarily represent the official views of the National Institutes of Health. Publisher Copyright: © 2022, Huazhong University of Science and Technology.
- [7] F. Lin, S. Shelton, D. Espindola, J. Rojas, G. Pinton, and P. Dayton, "3-d ultrasound localization microscopy for identifying microvascular morphology features of tumor angiogenesis at a resolution beyond the diffraction limit of conventional ultrasound," *Theranostics*, vol. 7, pp. 196–204, 01 2017.
- [8] M. R. Lowerison, N. C. Sekaran, W. Zhang, Z. Dong, X. Chen, D. A. Llano, and P. Song, "Aging-related cerebral microvascular changes visualized using ultrasound localization microscopy in the living mouse," *bioRxiv*, 2021. [Online]. Available: <https://www.biorxiv.org/content/early/2021/06/07/2021.06.04.447141>
- [9] A. Chavignon, V. Hingot, C. Orset, D. Vivien, and O. Couture, "3d transcranial ultrasound localization microscopy for discrimination between ischemic and hemorrhagic stroke in early phase," *Scientific Reports*, vol. 12, 10 2022.
- [10] C. Errico, J. Pierre, S. Pezet, Y. Desailly, Z. Lenkei, O. Couture, and M. Tanter, "Ultrafast ultrasound localization microscopy for deep super-resolution vascular imaging," *Nature*, vol. 527, 11 2015.
- [11] O. Viessmann, R. Eckersley, K. Christensen-Jeffries, M.-X. Tang, and C. Dunsby, "Acoustic super-resolution with ultrasound and microbubbles," *Physics in medicine and biology*, vol. 58, pp. 6447–6458, 09 2013.
- [12] K. Christensen-Jeffries, R. Browning, M.-X. Tang, C. Dunsby, and R. Eckersley, "In vivo acoustic super-resolution and super-resolved velocity mapping using microbubbles," *IEEE transactions on medical imaging*, vol. 34, 09 2014.
- [13] J. Kim, M. R. Lowerison, N. V. C. Sekaran, Z. Kou, Z. Dong, M. L. Oelze, D. A. Llano, and P. Song, "Improved ultrasound localization microscopy based on microbubble uncoupling via transmit excitation," *IEEE transactions on ultrasonics, ferroelectrics, and frequency control*, vol. 69, no. 3, pp. 1041–1052, 2022.
- [14] P. Song, J. D. Trzasko, A. Manduca, R. Huang, R. Kadirvel, D. F. Kallmes, and S. Chen, "Improved super-resolution ultrasound microvesSEL imaging with spatiotemporal nonlocal means filtering and bipartite graph-based microbubble tracking," *IEEE Transactions on Ultrasonics, Ferroelectrics, and Frequency Control*, vol. 65, no. 2, pp. 149–167, 2018.
- [15] X. Guo, D. Ta, and K. Xu, "Frame rate effects and their compensation on super-resolution microvessel imaging using ultrasound localization microscopy," *Ultrasonics*, vol. 132, p. 107009, 2023.
- [16] V. Hingot, C. Errico, B. Heiles, L. Rahal, M. Tanter, and O. Couture, "Microvascular flow dictates the compromise between spatial resolution and acquisition time in ultrasound localization microscopy," *Scientific Reports*, vol. 9, 02 2019.
- [17] B. Heiles, A. Chavignon, V. Hingot, P. Lopez, E. Teston, and O. Couture, "Performance benchmarking of microbubble-localization algorithms for ultrasound localization microscopy," *Nature Biomedical Engineering*, vol. 6, 05 2022.
- [18] O. Solomon, R. J. G. van Sloun, H. Wijkstra, M. Mischi, and Y. C. Eldar, "Exploiting flow dynamics for super-resolution in contrast-enhanced ultrasound," 2018, arXiv:1804.03134.
- [19] A. D. Bar-Zion, O. Solomon, C. Tremblay-Darveau, D. R. Adam, and Y. C. Eldar, "Sushi: Sparsity-based ultrasound super-resolution hemodynamic imaging," *IEEE Transactions on Ultrasonics, Ferroelectrics, and Frequency Control*, vol. 65, pp. 2365–2380, 2017.
- [20] J. Yu, L. Laverty, and K. Kim, "Super-resolution ultrasound imaging method for microvasculature in vivo with a high temporal accuracy," *Scientific Reports*, vol. 8, 09 2018.
- [21] X. Qian, H. Kang, R. Li, G. Lu, Z. Du, K. Shung, M. Humayun, and Q. Zhou, "In vivo visualization of eye vasculature using super-resolution ultrasound microvessel imaging," *IEEE Transactions on Biomedical Engineering*, vol. PP, pp. 1–1, 02 2020.
- [22] C. Huang, M. Lowerison, J. Trzasko, A. Manduca, Y. Bresler, S. Tang, P. Gong, U. W. Lok, P. Song, and S. Chen, "Short acquisition time super-resolution ultrasound microvessel imaging via microbubble separation," *Scientific Reports*, vol. 10, 04 2020.
- [23] R. J. G. van Sloun, O. Solomon, M. Bruce, Z. Z. Khaing, H. Wijkstra, Y. C. Eldar, and M. Mischi, "Super-resolution ultrasound localization microscopy through deep learning," *IEEE Transactions on Medical Imaging*, vol. 40, no. 3, pp. 829–839, 2021.
- [24] L. Milecki, J. Porée, H. Belgharbi, C. Bourquin, R. Damseh, P. Delafontaine-Martel, F. Lesage, M. Gasse, and J. Provost, "A deep learning framework for spatiotemporal ultrasound localization microscopy," *IEEE Transactions on Medical Imaging*, vol. PP, pp. 1–1, 02 2021.
- [25] D. Ackermann and G. Schmitz, "Detection and tracking of multiple microbubbles in ultrasound b-mode images," *IEEE Transactions on Ultrasonics, Ferroelectrics, and Frequency Control*, vol. 63, pp. 1–1, 11 2015.
- [26] T. Opacic, S. Dencks, B. Theek, M. Schulte, D. Ackermann, A. Rix, T. Lammers, E. Stickeler, S. Delorme, G. Schmitz, and F. Kiessling, "Motion model ultrasound localization microscopy for preclinical and clinical multiparametric tumor characterization," *Nature Communications*, vol. 9, 04 2018.
- [27] J. Yan, T. Zhang, J. Broughton-Venner, P. Huang, and M.-X. Tang, "Super-resolution ultrasound through sparsity-based deconvolution and multi-feature tracking," *IEEE Transactions on Medical Imaging*, vol. PP, pp. 1–1, 02 2022.
- [28] E. H. Georgoulis, J. Levesley, and F. Subhan, "Multilevel sparse kernel-based interpolation," *SIAM Journal on Scientific Computing*, vol. 35, no. 2, pp. A815–A831, 2013.
- [29] H. Jalilian, S. Afrakhteh, G. Iacca, and L. Demi, "Increasing frame rate of echocardiography based on a novel 2d spatio-temporal meshless interpolation," *Ultrasonics*, vol. 131, p. 106953, 2023.
- [30] C. Demené, T. Deffieux, M. Pernot, B.-F. Osmanski, V. Biran, S. Franchi-Abella, J.-M. Correas, I. Cohen, O. Baud, and M. Tanter, "Spatiotemporal clutter filtering of ultrafast ultrasound data highly increases doppler and fultrasound sensitivity," *IEEE transactions on medical imaging*, vol. 34, 04 2015.
- [31] K. Christensen-Jeffries, S. Harput, J. Brown, P. N. T. Wells, P. Aljabar, C. Dunsby, M.-X. Tang, and R. J. Eckersley, "Microbubble axial localization errors in ultrasound super-resolution imaging," *IEEE Transactions on Ultrasonics, Ferroelectrics, and Frequency Control*, vol. 64, no. 11, pp. 1644–1654, 2017.
- [32] D. Espindola, R. DeRuiter, F. Santibanez, P. Dayton, and G. Pinton, "Quantitative sub-resolution blood velocity estimation using ultrasound localization microscopy ex-vivo and in-vivo," *Biomedical Physics & Engineering Express*, vol. 6, 03 2020.
- [33] H. W. Kuhn, "The hungarian method for the assignment problem," *Naval Research Logistics (NRL)*, vol. 52, no. 1, pp. 7–21, 2005.
- [34] Y.-H. Nai, B. W. Teo, N. L. Tan, S. O'Doherty, M. C. Stephenson, Y. L. Thian, E. Chiong, and A. Reilhac, "Comparison of metrics for the evaluation of medical segmentations using prostate mri dataset," *Computers in Biology and Medicine*, vol. 134, p. 104497, 2021.
- [35] V. Hingot, A. Chavignon, B. Heiles, and O. Couture, "Measuring image resolution in ultrasound localization microscopy," *IEEE Transactions on Medical Imaging*, vol. 40, no. 12, pp. 3812–3819, 2021.

- [36] M. van Heel and M. Schatz, "Fourier shell correlation threshold criteria," *Journal of Structural Biology*, vol. 151, no. 3, pp. 250–262, 2005. [Online]. Available: <https://www.sciencedirect.com/science/article/pii/S1047847705001292>
- [37] W. Saxton and W. Baumeister, "The correlation averaging of a regularly arranged bacterial cell envelope protein," *Journal of microscopy*, vol. 127, no. 2, pp. 127–138, 1982.
- [38] A. SScott and E. J. Kansa, "Multiquadric radial basis function approximation methods for the numerical solution of partial differential equations," *Advances in Computational Mechanics*, vol. 2, no. 1–220, p. ., 2009.
- [39] P. Assari, H. Adibi, and M. Dehghan, "A numerical method for solving linear integral equations of the second kind on the non-rectangular domains based on the meshless method," *Applied Mathematical Modelling*, vol. 37, pp. 9269–9294, 2013.
- [40] C. Micchelli, "Interpolation of scattered data: Distance matrices and conditionally positive definite functions," *Constructive Approximation*, vol. 2, pp. 11–22, 1986.
- [41] R. Hardy, "Multiquadric equations of topography and other irregular surfaces," *J. Geophys. Res.*, vol. 176, pp. 1905–1915, 1971.
- [42] R. Franke, "Scattered data interpolation: test of some methods," *Math. Comput.*, vol. 38, pp. 181–200, 1982.
- [43] H. Wendland, "Scattered data approximation," *Cambridge University Press*, p. ., 2005.

## APPENDIX

### A. Interpolation matrix invertibility

In order to deal with a well-posed interpolation problem, the matrix  $\Phi$  in Eq. (5) must be invertible. We discuss the invertibility of the **interpolation matrix for GA and MQ functions** [38] since these two are the RBFs that are used in this work.

**Definition 1:** The following conditions should be satisfied to have a positive definite function  $\phi$  on the domain  $\mathbb{R}^d$ . Firstly, the function  $\phi$  must be even. Secondly, the following condition should be fulfilled for all the points  $\mathbf{X}_1, \mathbf{X}_2, \dots, \mathbf{X}_N$  and any vector  $\mathbf{v} = [v_1, v_2, \dots, v_N]^T$ :

$$\sum_{i=1}^N \sum_{j=1}^N v_i v_j \phi(x_i - x_j) \geq 0. \quad (11)$$

**Remark:** The function  $\phi$  is strictly positive definite if and only if the null vector is the only vector  $\mathbf{v}$  that converts the inequality in Eq. (11) into an equivalence.

Since all of the eigenvalues of the interpolation matrix  $\Phi$  are positive with a strictly positive definite  $\phi$ ,  $\Phi$  is positive definite and thus invertible.

**Theorem 1:** The function  $\phi$  is absolutely monotone on  $[0, \infty)$  if it meets the following conditions [39]:

- $\phi \in C[0, \infty)$
- $\phi \in C^\infty(0, \infty)$
- $(-1)^l \phi^{(l)}(r) \geq 0$  where  $r > 0$  and  $l = 0, 1, \dots$

**Theorem 2:** If a function  $\phi$  is completely monotone on  $[0, \infty)$ , but not constant, then  $\phi(\|\cdot\|^2)$  is strictly positive definite and a radial basis on  $\mathbb{R}^d \forall d$  [39].

**Remark 1:** The GA function is absolutely positive definite in accordance with Theorems 1 and 2, which makes its interpolation matrix invertible. Additionally, a condensed version of the Micchelli theorem [40], which ensures the invertibility of the MQ interpolation matrix, is given in [38].

**Remark 2:** Despite the invertibility of matrix  $\Phi$ , a high

condition number of this matrix may still render the interpolation problem ill-posed. As a consequence, we must choose the appropriate  $\tau$  parameter in order reduce the error. The parameter  $\tau$  can be set using a variety of methods, such as the Hardy [41] and the Frank [42] approaches. It should be noted that the  $\tau$  value is typically chosen at random in the literature, based on the interpolation matrix condition number.

### B. Error analysis

The rate of convergence (*RoC*) of the RBF technique for adequately smooth functions is exponential (e.g., the *RoC* for MQ is  $O(\mathfrak{S}^N)$ , where  $0 < \mathfrak{S} < 1$ ). However, for other methods, including the finite differences and polynomial spline bases, the *RoC* is in the order of  $O(N^{-m})$  for a given constant  $m$ .

The MQ technique exponentially converges to proper smooth functions for a particular shape parameter value ( $\tau$ ). In this case,  $h$ , i.e., the distance between  $\mathbf{X}$  and  $\mathbf{X}_j$ , is reduced to its minimum upper bound:

$$h = \sup_{\mathbf{X} \in \Gamma} \left( \min_{\mathbf{X}_j^c \in \Xi} \|\mathbf{X} - \mathbf{X}_j^\tau\| \right) \quad (12)$$

where  $\Gamma$  indicates a series of centers and  $\Xi$  represents the interpolation space. Therefore, we can formulate the interpolation error as follows:

$$|f(\mathbf{X}) - S(\mathbf{X})| \leq e^{-\frac{K\tau}{h}}. \quad (13)$$

In the other points (i.e., the middle points), the error is expressed as:

$$|f(\mathbf{X}) - S(\mathbf{X})| \leq K \mathfrak{S}^{\frac{1}{\tau h}}. \quad (14)$$

The same findings are obtained for the GA basis in [43].